QUANTIFYING SNOW WATER EQUIVALENT USING TERRESTRIAL GPR AND UAV PHOTOGRAMMETRY

Running title: Snow Water Equivalent Retrieval

Semih Yildiz[1*], Zuhal Akyurek[1,2], Andrew Binley[3]

[1] Department of Geodetic and Geographic Information Technologies, Middle East Technical University, Ankara, Turkey

[2] Department of Civil Engineering, Middle East Technical University, Ankara, Turkey

[3] Lancaster Environment Centre, Lancaster University, Lancaster, United Kingdom

*Corresponding Author:

Email: semih.yildiz@metu.edu.tr

Acknowledgements

This study was partly funded by TUBITAK (The Scientific and Technological Research Council of Turkey) in the scope of research and development project 115Y041 and fieldworks were performed in cooperation with the General Directorate of State Hydraulic Works, Turkey. The authors would like to thank The General Directorate of State Hydraulic Works personnel for their support and assistance in the fieldworks. The comments from Adam R. Mangel and an anonymous reviewer on an early version of the manuscript helped improve the manuscript.

Abstract

This study demonstrates the potential value of a combined UAV Photogrammetry and ground penetrating radar (GPR) approach to map snow water equivalent (SWE) over large scales. SWE estimation requires two different physical parameters (snow depth and density), which are currently difficult to measure with the spatial and temporal resolution desired for basin-wide studies. UAV photogrammetry can provide very high-resolution spatially continuous snow depths (SD) at the basin scale, but does not measure snow densities. GPR allows nondestructive quantitative snow investigation if the radar velocity is known. Using photogrammetric snow depths and GPR two-way travel times (TWT) of reflections at the snow-ground interface, radar velocities in snowpack can be determined. Snow density (RSN) is then estimated from the radar propagation velocity (which is related to electrical permittivity of snow) via empirical formulas. A Phantom-4 Pro UAV and a MALA GX450 HDR model GPR mounted on a ski mobile were used to determine snow parameters. A snow-free digital surface model (DSM) was obtained from the photogrammetric survey conducted in September 2017. Then, another survey in synchronization with a GPR survey was conducted in February 2019 whilst the snowpack was approximately at its maximum thickness. Spatially continuous snow depths were calculated by subtracting the snow-free DSM from the snow-covered DSM. Radar velocities in the snowpack along GPR survey lines were computed by using UAV-based snow depths and GPR reflections to obtain snow densities and SWEs. The root mean square error of the obtained SWEs (384 mm average) is 63 mm, indicating good agreement with independent SWE observations and the error lies within acceptable uncertainty limits.

Key words: Digital Surface Model, Digital Terrain Model, Ground Penetrating Radar, Photogrammetry, Snow Density, Snow Tube, Snow Water Equivalent, Unmanned Aerial Vehicle.

1 Introduction

Snow water equivalent (SWE) is the product of snow depth and bulk density (relative to water) and is commonly reported in units of mm. It is a key variable that characterizes the hydrological significance of the snow cover. SWE information is needed to calibrate hydrological models, estimate snowmelt runoff in drainage basins, and improve decision making concerning water supply, hydroelectric power and flood forecasting. SWE is also useful to studies related to snow climatology, ecological function, and avalanche forecasting. SWE can exhibit substantial spatiotemporal heterogeneity due to a range of effects such as wind, temperature, topography, and canopy structure. The measurement of snow depth alone is not sufficient to obtain SWE since snow density also exhibits high spatiotemporal variations over a basin (Gray et al., 1970). Estimating the spatial distribution and temporal evolution of SWE in mountain basin is currently considered as one of the most important unsolved problems in snow hydrology (Capelli et al., 2019).

SWE is typically measured directly using a snow core (Church, 1933; Goodison et al., 1987; Dixon and Boon, 2012). However, such an approach is labor intensive for frequent sampling, destructive, prone to human error and can only be performed at accessible locations (Pomeroy and Gray, 1995). A more labor-intensive process for SWE estimation is the digging of a snow pit (e.g., Elder et al., 1998). Snow pits are usually used for research purposes and can only be applied at a location once due to its destructive nature. The snow pillow is another SWE measurement instrument, which has been used since the 1960s (Beaumont, 1965) to provide an automated direct estimate of SWE by measuring the pressure due to the mass of overlying snow. Snow pillows are subject to diurnal measurement errors, logistical and transportation issues with respect to installation, can only measure a surface area of about 10 m^2, and are prone to bridging errors due to the formation of ice lenses (Osterhuber et al., 1998; Johnson and Schaefer 2002).

Down-looking Ground Penetrating Radar (GPR) has the potential to provide laterally and spatially continuous estimates of SWE (Eisen et al., 2003; Harper and Bradford, 2003; Marshall et al., 2005; Godio, 2009; Bradford et al., 2009, Gustafsson et al., 2012; Forte et al., 2014; Holbrook et al., 2016, Webb, 2017). GPR is extremely portable; sensors can be pulled behind an operator on snowshoes (e.g., Bradford et al., 2009), towed behind ski mobiles (e.g., Gacitua et al., 2013), and flown from helicopters (e.g., Sold et al., 2013) or drones (e.g., Jenssen et al., 2018). A GPR transmits electromagnetic energy into the snowpack. A significant impedance contrast typically occurs at the snow/ground interface and produces an easily identifiable reflection (Bradford et al., 2009). GPR data provide accurate measurements of the two-way travel time (TWT) of EM waves reflected from boundaries within, and at the base of, the snow layer. The essential prerequisite of determining the SWE via GPR is the knowledge of the velocity of electromagnetic radiation emitted into the investigated snow cover. The radar velocity at any position is needed to convert the TWT records into SWE. Typically, the radar velocity is estimated from common mid-point (CMP) measurements (Harper and Bradford, 2003). However, collecting CMPs can be time consuming and requires separable antennas. GPR measurements are usually made in a common offset (CO) configuration, providing profiles reflections. In such a configuration, the radar velocity can be estimated from diffraction hyperbolas as localized anomalies are passed along the survey line (Moore et al. 1999). Bradford and Harper (2005) utilized migration velocity analysis (MVA) (seeking to place reflected energy at its point of origin) of low-frequency (25 MHz) radar data to determine the density of glacial ice. Holbrook et al. (2016) applied a similar MVA algorithm to high-frequency (800 MHz) GPR data to estimate average dry snowpack density in a mountain watershed. However, the common methods of visually inspecting migrated images or fitting curves to diffraction hyperbolas are time-consuming and subject to human error. Thus, St. Clair and Holbrook (2017) developed a semi-automatic processing flow for measuring GPR velocity from CO data applying MVA presented by Fomel et al. (2007). The main disadvantages of such an approach are related to the accuracy and resolution, since only few hyperbolas can usually be analyzed and they are irregularly distributed along the transects. In practice, there are many cases where exploiting the curvature of diffraction hyperbolas are not feasible or unreliable, thus the evaluation of the wave velocity may require support from an independent method. Several studies have shown that independent measurements of wave velocity can be performed using Time Domain Reflectometry (TDR) (Harper and Bradford, 2003; Previati et al., 2011; Di Paolo et al., 2015). Alternatively, Webb (2017) used snow pillow measurements and snow pits to calibrate the GPR wave velocity estimates. While the joint use of GPR with external methods like TDR probes, snow pits or snow pillows is capable of estimating snow EM wave velocity, such measurements are spatially discrete and can only be used to represent the average wave velocity for the study plot. Webb et al. (2018) combined GPR with terrestrial LIDAR scanning and snow pits to estimate the spatial distribution of liquid water content. Terrestrial LIDAR conveniently measures snow depths at the catchment with steep slopes, however, it is still prohibitively expensive in most countries.

Unmanned aerial vehicle (UAV) based digital photogrammetry (UAV photogrammetry) is emerging as a potential low-cost technique to yield spatially continuous snow depth measurements (Avanzi et al. 2018; Harder, Schirmer, Pomeroy, & Helgason, 2016; Bühler et al., 2016). UAVs are flexible platforms in terms of acquisition time and region of interest (Whitehead et al., 2014). They can be used to acquire images of the study area with optical cameras having cm scale ground resolution (Avanzi et al. 2018). These images are processed using digital image processing and structure from motion (SfM) algorithms. The output is a very high-resolution digital surface model (DSM) of the survey area. Snow depths of the study area are obtained by simply subtracting a snow-free DSM from a snow-covered DSM.

Two well-established methods that have yet to be combined are GPR and UAV photogrammetry. In this study, we show how photogrammetric snow depths can be combined with measurements of dielectric properties of the snowpack from a CO GPR system to fully exploit the benefits of each in SWE measurements. We believe that this is the first time these measurements have been combined to nondestructively derive the spatial distribution of SWE in dry snow conditions. To demonstrate the approach two datasets of GPR survey were collected concurrently with UAV photogrammetry based snow depths at a study site in Turkey. The first data set was collected by pulling the GPR on the snow surface along a pre-determined transect; the second one was collected with the GPR antenna mounted on the side of a ski mobile. SWE was derived from the product of obtained snow density and snow depth. One of the motivations in this study is to answer the question: How accurately can SWE be characterized by combining UAV Photogrammetry and GPR approach? To validate the methods, we compare snow depth, density and SWE estimations with manual observations along transects.

2 Methods

2.1 Site description and instrumentation

The study area is the Ilgaz Mountains National Park catchment located in the northwest of Turkey. The catchment is bordered in the north by Gökırmak River and in the south by Devrez Creek, forming the hydrographic boundary between the two river basins. The peak altitude of the mountains is 2587 m above mean sea level (MSL). The catchment has a surface area of approximately 45 km^2 and generally composed of schists and volcanic rocks. The area is located in a transitional zone between two of macro climate regions in Turkey (steppe climate of Inner Anatolia region and oceanic climate of Black Sea region). The land mainly consists of forest and open forest areas where pure Fir and Scotch pine stands. The alpine zone beginning from 2000–2200 m above MSL is ecologically rich, consisting of rare and endemic vegetation formed by dwarf shrubs.

The experimental plot is approximately 1 ha for GPR surveys and 7 ha for UAV photogrammetry surveys. Vegetation on the plot consists of tree cover and dwarf shrubs. The test site has predominantly south and west facing aspects and an average 13° slope angle with a mean elevation of about 2000 m above MSL. Having a mountainous and rugged terrain structure with different land cover makes this test area important for location-dependent applications. The site has continuous observations of snow depth and air temperature adjacent to the experimental plot. The annual mean air temperature is 5.7 °C. The study area has a snow-dominated runoff regime with the highest runoff volume during spring caused by melting snow. The test area is accessible during both winter and summer seasons. Figure 1a highlights canopy heights, slope and aspects of the terrain, elevation contours, where GPR data were collected, as well as the location of the ultrasonic sensor and snow core survey points. An overview of the site is provided in Figure 1b. The site was chosen on account of its good accessibility, and well-established infrastructure (e.g., power supply and network connection).

Figure 1 Here

There is an ultrasonic snow depth sensor (Campbell SR50A model) operated by the Directorate of State Hydraulic Works (DSI) that measures the snow depth at a single point in the study area during the winters. The monthly snow depths in the basin for the 2019 water year is shown in Figure 1b. The maximum depth was recorded as 141 cm on 17 January 2019.

2.2 Snow Depth (SD) Quantification via UAV Photogrammetry

The first UAV photogrammetry mission was carried when there was no snow cover in the plot area using a DJI Mavic Pro model UAV with a compact 12 MP DJI FC220 model camera. The mission was performed in winter conditions using a Phantom-4 model UAV with an integrated 12.4 MP DJI FC330 model camera. Both UAVs are lightweight and easily transported to/from the site. A combination of on-board navigation sensors (GNSS, Inertial Measurement Unit, IMU, barometer and compass) and an adaptive control unit permit high positional accuracy and stable flight characteristics (DJI, 2017a). According to the DJI official website, both UAVs have hover accuracy range of better than ±0.5 m in vertical and ±1.5 m in horizontal (DJI Official, 2021a; DJI, 2021b).

All images were captured in the visible (400–700 nm) part of the electromagnetic spectrum and saved in RGB color model. The specifications of the UAVs, cameras and defined flight parameters are listed in Table 1.

Table 1 Here

The first photogrammetric flight was performed on the morning of 7 September 2017 (a clear and sunny day) considering the drone specifications and law regulations. A flight plan was designed and UAV parameters were defined for the study area using UgCS software (Table 1). Eleven homogeneously distributed ground control points (GCPs) were established, marked with paint and positioned with a high precision RTK GNSS at ITRF96 TM-33 projection coordinate system. The flight mission was successfully done and 118 images in total were gathered. The second field campaign was carried out on 5 February 2019. The survey time was selected according to prior snow observations and weather conditions to be sure that seasonal snow was dry and had reached its peak thickness. Although snow data of the previous years at the test area show that the maximum snow depth typically reaches in March during the year, we decided to perform the survey at the beginning of February due to the likelihood of wet snow conditions in March. The sky was cloud-free and air temperature was under zero degrees. The sensible temperature, due to relative humidity and wind, was -3 °C; air pressure was 1013.0 mbar and relative humidity was 87%. For the winter field campaign, flight parameters were defined as listed in Table 1. The number of images, the height of flight and the overlapping rates were increased in the winter flight to successfully model the snow-covered area. A base station and seven homogeneously distributed GCPs were established in the field, marked with pre-made corrugated plastic sheets and positioned with high precision GNSS at ITRF96 TM-33 projection coordinate system. GNSS measurements were made using two FOIF model GNSS units, one as a base and the other as a rover. A base GNSS was located on a pre-established point belong to national geodetic network to increase the positional accuracy. The flight resulted in the record of 120 images.

The Pix4D Mapper (version 4.3.27) software was used to process data collected via UAV photogrammetry. Georeferenced 2D maps (orthophotos) and 3D models (DSMs and Digitial Terrain Models (DTMs)) were obtained in three steps: initial processing, point cloud densification, and model generations. UAV datasets were successfully processed satisfying the quality specifications defined by the Pix4D software community. Models were georeferenced using 3D Ground Control Points (GCPs). Noise filtering and sharp type surface smoothing were applied to the DSMs. Overall, two DSMs, two DTMs and two orthoimages were generated from the field surveys. Absolute accuracy of a photogrammetric project is defined by the difference between the location of features on the reconstructed model and their true position in a certain reference frame. In order to derive absolute horizontal and vertical accuracies, the location of 3D GCPs on the reconstructed model and their true position values on the ground were compared with each other.

Table 2 Here

The absolute accuracy of the derived DSMs (snow-free and snow-covered maps), relative to the GCPs are summarized in Table 2. The created snow-free DSM and snow-covered DSM were then clipped (120 m x170 m) and resampled with resolution of (6 cm x 6 cm) to focus on the GPR survey area. Snow depths (SD) were calculated by subtracting snow-free DSM from snow-covered DSM.

2.3 Ground Penetrating Radar Measurements

Two-way-travel time (TWT) of GPR waves through snow were obtained on the same day as the UAV based photogrammetric surveying. We used a pulse type GPR system with a shielded antenna (MALÅ GX450 HDR. Basic data parameters (depth/time window, time gain, velocity of the under layer, triggering options (wheel, time or keyboard), wheel type, and point interval) were set up prior to the data acquisitions. Distances along the GPR surveys were measured using a wheel odometer. The wheel was calibrated along a 10 m long distance of snow surface before GPR data acquisitions. GPR antenna was mounted on a plastic sledge. Three different GPR lines were acquired to observe effects on GPR measurements in different configurations and topographic conditions. The plastic sledge was placed directly on the snow surface and dragged along the GPR survey lines. In one configuration, the GPR was dragged manually by the operator at walking speed along two perpendicular transects named Line-1 and Line-2. In another configuration, the GPR was dragged via ski mobile to survey a longer transect. The latter transect was named Ski Mobile Path. All survey transects (Line-1, Line-2 and Ski Mobile Path) are shown in Figure 1b.

GPR acquisition parameters were defined to obtain 140 TWT samples per trace leaving 0.0076 m distance interval between each traces. The optimal step size is 1/4 wavelength. Our system acquired data at a significantly higher density so we binned the data into 1/4 wavelength size bins and stacked the traces within those bins. 140 samples having a 0.3125 ns time interval results in a 43.75 ns time-window. Line-1 is 89 m and Line-2 is 99 m long. Surveying each of the lines took approximately 3 minutes. The speed of the operator was about 0.5 m/sec. A GNSS antenna registered location information at 5 m intervals along the transects. The rest of the traces in between these intervals were linearly interpolated assuming that the operator was walking straight between each of consecutive GNNS points.

Manually pulling the GPR to measure snow parameters is possible for short transects. Thus, the GPR mounted plastic sledge was tied to the tip of an aluminum rod mounted to the ride side of a Yamaha VK540 model ski mobile. Dragging the GPR antenna about 1m to the side of the ski mobile ensured that measurements are taken on pristine snow whilst allowing for maximum mobility to cover longer transects. The average speed of the ski mobile was 2.2 m/sec; attempts were made not to exceed 5m/sec. Although the GPR has an inbuilt DGPS (EGNOS, +/- 1.5 m), its accuracy was considered poor for the survey, thus an external RTK GNSS (+/-1 cm) was used. The external GNSS positions recorded once per second fixed to the rear of the ski mobile and was integrated into the GPR acquisition system. The offsets between GNSS antenna and GPR antenna were geometrically corrected by matching up the GNSS data time with the GPR trace time. GPR acquisition parameters were defined as: 140 TWT samples per trace; 0.078 m distance interval between each traces; 43.75 ns time-window. The survey started at 14:33 and finished at 14:41, covering a distance of 1043 m.

Reflexw (version 8.0.2) software was used to process the GPR datasets. The quality of the radar data was very good for the entire data sets. Snow/ground interfaces are well detectable in each section even without any gain applied, due to the very low signal attenuation of the snow. Several basic steps were applied. (1) Time zero was manually determined and used to correct the time readings. (2) A manual gain function was used to apply a time gain to compensate the signal attenuation. (3) A Butterworth band-pass filter with lower cut (225 MHz) and upper cut (675 MHz) was utilized to reject out parts of the signal corresponding to irrelevant frequencies. (4) System based coherent noise was eliminated using a background removal filter. Given the series of filtered traces, the auto-pick function was used to quickly and objectively detect and characterize snow-ground boundary reflections along the GPR profiles.

2.4 Snow Water Equivalent (SWE) Estimation

Maxwell's Equations (Balanis, 1989) describe the propagation of electromagnetic energy as a coupled process between electrical and magnetic forces and fluxes. The effective dielectric permittivity (ε) of snow is sensitive to snowpack density and liquid water content (Bradford et al., 2009; Heilig et al., 2010). The dielectric permittivity of dry snow can be calculated from the observed velocity (v) of the radar wave through snow (e.g., Mitterer et al., 2011). The dielectric permittivity of dry snow has a nearly loss-free dielectric permittivity and independent of frequency from about 1 MHz up to the microwave range of at least 10 GHz (Matzler, 1996). Under the assumptions of low loss and negligible magnetic susceptibility, the velocity, v, is equal to:

$$v = \frac{c}{\sqrt{\varepsilon}} \tag{1}$$

where c is speed of light in vacuum and ε is relative dielectric permittivity.

In dry snow (no liquid water), the radar velocity depends only on the relative proportions of air and ice and their dielectric permittivity, and snow density can be determined solely from the radar velocity (Denoth et al., 1984, Mätzler, 1996). In this study, we assumed that the snow was dry because the temperature of the survey area for several days prior to the survey was mostly below zero Celsius degrees. The observed radar velocities and calculated snow densities were compared with the study of Bradford et al. (2009). The results are consistent with dry snow conditions having zero snow water content. The radar velocity for the underlying snowpack was calculated using UAV photogrammetry based SD and GPR TWT:

$$v = \frac{2\ x\ SD}{TWT} \tag{2}$$

where SD is the snow depth, TWT is the GPR two-way travel time and v is the radar velocity in the snow layer. The obtained velocity was converted to permittivity which is based on the relationship between radar velocity, speed of light (c) and permittivity using equation (1). Permittivity is a complex quantity (i.e., $\varepsilon = \varepsilon' + i\varepsilon''$). In dry snow, $\varepsilon'' \approx 0$ (Bradford et al., 2009). The literature reports many variants of mixing models to relate the snow density and permittivity. We used an empirical equation suggested by Tiuri et al. (1984) for dry snow conditions:

$$\varepsilon' = 1 + 1.7\rho + 0.7\rho^2 \tag{3}$$

where ρ is snow density in g/cm^3 and ε' is the real component of the snow permittivity. Then, the snow water equivalent can be obtained from multiplying SD with snow density (ρ):

$$SWE = SD\ x\ \rho \tag{4}$$

The main procedure for quantifying snow characteristics based on combined UAV photogrammetry -GPR measurements is summarized as a flow chart in Figure 2.

Figure 2 Here

2.5 Manual measurements for validation

Snow depths, densities and snow water equivalents along Line-1 and Line-2 were also manually measured using a snow sampler (a Mountain Rose type tube) to assess the accuracy of snow measurements obtained from UAV Photogrammetry and GPR. It is made of a 1.2 m long aluminum tube and has a cross-sectional area of 30 cm2. A scaled metric system marked on the tube allows the operator to read snow depth after penetrating it into the snowpack. Water content was calculated by weighing the tube before and after taking a sample. Operation of the Mountain Rose type snow tube is prone to errors due to the condition of the snow mass and the experience of the person performing the measurement (Goodison, 1978). Measurements were performed at 5 to 10 m (on average) distances between each sequentially sampled points. There were 14 points measured along Line-1 and 13 points along Line-2 as shown in Figure 1b. Each of these points was positioned via RTK GNSS.

3 Results

3.1 SD Retrieved from UAV Photogrammetry

It is straightforward to compute snow depths (SD) in canopy free areas by simply subtracting the snow-free DSM from the snow-covered DSM. However, in vegetated areas the task is less straightforward. The vegetation at the base of the snow cover leads to a systematic underestimation of SD mapped with photogrammetry as well as a systematic overestimation of SD measured manually with the snow tube because the tube penetrates the snow-free bottom layer (Bühler et al, 2016). The “real” SD is most probably a value between the manual and the photogrammetric measurements. Taking this into consideration, we estimated SD based on both snow-free DSM and snow-free DTM models to partially overcome vegetation effects. A DSM represents the elevation of terrain as well as above-ground features such as trees, vegetation and human made objects whereas a DTM represents the elevation of bare terrain where above-ground features are removed.

Figure 3 Here

Snow depths from the top of canopies (SDC) and bare ground were calculated by subtracting the snow-free DSM from snow-covered DSM. Snow depths from top of terrain (SDT) were calculated by subtracting snow-free DTM from snow-covered DSM. The terms SDC, SDT, HC, DSM, and DTM are illustrated in Figure 3. Snow depths were estimated for canopy-free regions (HC< 7 cm) and used as control data. The corresponding pixel couple of SDC and SDT were compared and the one closer to the mean snow depth of the control data was assigned as the correct SD value. Snow depths (SDs) were modelled for the study area as shown in Figure 4.

Figure 4 Here.

3.2 SWE Estimation

i. Along Transect

GPR surveys along Line-1 and Line-2 provided two-way travel time (TWT) in nanosecond units at 0.7cm intervals. Figure 5 illustrates the effectiveness of the GPR snow observations. The GPR was operated on the snow surface; an inclined snow surface creates tilting and rolling effects on the GPR antenna. Thus, SD and TWT need to be collocated. The collocation procedure was done for each of the SD pixels before velocity calculation. Both zenith angle (compliment of slope angle) of summer and winter surfaces were calculated for each of the SD pixels. Then, SD was collocated to TWT using trigonometry. Then, the radar velocity for each pixel along transects was calculated based on collocated SD and TWT parameters. According to the empirical formula suggested by Tiuri (1984), the EM wave velocity can be in the range 17.5 cm/ns to 30 cm/ns. In canopy regions, apparent snow depths can be affected by vegetation cover. Thus, velocity values which are not in this range due to the vegetation cover were eliminated from the data. Then, velocities in the specified range were converted to snow densities. SWE values were calculated for each SD pixels lying on the GPR survey profiles by multiplication of SD with RSN (Figure 6).

Figure 5 Here

Figure 6 Here

ii. Raster based

Snow velocities and densities along ski mobile transects were calculated following the procedure applied to the transect lines (Line-1 and Line-2) mentioned in the previous section. GPR traces were matched up with

GNSS points based on trace time and position record time. GNSS records positions once per seconds leading 20 cm to 60 cm distances between each consecutive points depending on speed of ski mobile.

Variograms of the snow densities along Line-1 and Line-2 were created to test whether interpolation is suitable to obtain spatially distributed RSN over large areas (Figure 7a and Figure 7b). The range distances show that the spatial correlation for Line-1 is about 7 m while for Line-2 is about 2.5 m. Average slope along Line-1 is 5% and along Line-2 is 12%. This suggests that the spatial correlation along a transect is slope dependent. The spatial correlation of snow density along the ski mobile survey (Ski Mobile Path) is about 7.5 m (Figure 7c). Densities obtained from the transect UAV-GPR survey model (Line-1, Line-2 and Ski Mobile Path) were interpolated over the area using the inverse distance weighting algorithm (IDW) to get continuously distributed snow density (Figure 8b). In total 3225 points were interpolated in the survey area. Finally, raster snow water equivalent was obtained from mathematical product of raster SD and raster RSN (Figure 8c).

Figure 7 Here

Figure 8 Here

3.3 Uncertainties in SWE estimations

One of the motivations in this study is to answer the question: How accurately can SWE be characterized by combining UAV Photogrammetry and GPR? A spatially varying uncertainty ($\boldsymbol{\sigma}_{SD}$) in the photogrammetric snow depths can be expressed by estimating the root mean squared error (RMSE) of the propagated error for each grid cell

$$\sigma_{SD}^2 = \sigma_{on}^2 + \sigma_{free}^2 \tag{5}$$

where σ_{on} and σ_{free} are measures of uncertainty for the snow-covered DSM and snow-free DSM, which are assumed to be independent. The RMSE was used to determine the accuracy of the DSMs and the snow depths from the GNSS-surveyed validation data. The uncertainty in the DSMs was estimated by calculating the RMSEs (σ) in elevation for each grid cell from high precision GNSS surveys done at the GCP locations during UAV surveys. The RMSE of the snow-free DSM is ±5.1 cm while the RMSE of the snow-covered DSM is ±4.3 cm (Table 1). The smoother snow-covered DSM surface heights have a higher accuracy than the snow-free DSM height. The accuracy of the DSMs is expected to decrease where the terrain surface has a higher slope, is rougher (i.e., rocky debris cover), and further away from ground control points. The accuracy of the elevation values is spatially more heterogeneous in the snow-free DSM than in the snow-covered DSM. Finally, the overall uncertainty in the calculated SD is obtained as ±6.7 cm by using equation (5). Intuitively, we expect that the accuracy of a radar travel time picked from a radiogram is related to the frequency of the arrival and the signal-to noise ratio (SNR). Aki and Richards (1980) presented this in a formula (6) to quantify such accuracy:

$$\Delta t_{max} = \frac{1}{f_m log_2(1+(SNR)^2)} \tag{6}$$

where Δt_{max} is the uncertainty in travel time, f_m is the central frequency of the wave, SNR is the signal-to noise ratio. The GPR used in this study has 450 MHz central frequency and 101dB SNR. Accordingly, the uncertainty in the radar travel time is calculated as 0.16688 ns. Bentley and Trenholm (2002) used the same formula and calculated a priori estimate of uncertainties in their travel time as of 0.91 ns for 200 MHz data and 1.82 ns for 100 MHz data.

Strong snow/ground reflections show that GPR accurately detects snow depths. However, small bushes, mainly alpine rose, juniper and erica, rising up to 50 cm above ground in summer are pressed down to the ground by the snowpack but form a snow-free layer at the bottom of the snowpack which can have a depth of a few centimeters to decimeters (Feistl et al., 2014). Such layers may lead to some uncertainties in GPR TWT but they are not possible to quantify with current data sets. Both uncertainties in SD and TWT, which are independent to each other, lead to a total uncertainty of ±84 mm in SWE.

3.4 Validation of SWE estimations

Snow tube measurements were considered as a control measure set to evaluate the accuracy of snow depth (SD), snow density (RSN) and snow water equivalent (SWE) estimations derived from the combined photogrammetry and GPR methods. Manual snow measurements were assumed as true values though they inherently include some errors. Both snow tube and GPR measures snow properties from the top of the terrain even in canopy-covered areas. However, UAV surveys observe snow depths from the top of the terrain in canopy-free areas and from top of the canopies in canopy cover regions. Although the use of a DTM model partially solves the canopy effects, there may still be some deviations in SD values located in canopy covered regions. SWE measurements along the transect may differentiate from raster SWE values since IDW interpolation is just an approximation to the actual value rather than a measure of it. Also, in canopy covered regions, a transect model uses average velocity (both TWT and photogrammetric SD) as a reference to attain the SDC or SDT pixels, while raster model uses average snow depth (only photogrammetric SD). Thus, accuracy measurements were done based on whether points were located in canopy-covered areas or not for both transects and raster model. Although 27 points were measured via snow tube, 4 of them were located on complex canopy where UAV-photogrammetry failed to get snow depths. Among the remaining 23 different points sampled at 5m intervals, 8 of them are still located in canopy-covered regions where UAV photogrammetry was able to measure SD. The detail comparisons of the snow depths, snow densities and snow water equivalents obtained from suggested models and snow tube are presented in Figure 9.

Snow depths (SD) obtained along transects (Line-1 and Line-2) based on GPR TWTs (mean value is 106 cm) were compared with snow depths measured manually with a snow tube (mean value is 104 cm) (Table 3). The root mean squared error (RMSE) of the residuals is ±6 cm which is consisting with model accuracy (± 6.7 cm). The overall RMSE of the raster SD is (± 9 cm) which is higher than the expected photogrammetric SD uncertainty (± 6.7 cm). However, the overall accuracy includes canopy effects. Achieving ± 9 cm uncertainty given tens of cm canopy heights suggests that the approach is very promising. The average snow depth measured by the ultrasonic sensor from 12:00 to 14:00 on the date of fieldwork was 125 cm. When this value is compared with the one obtained from UAV photogrammetry (126 cm), it is possible to say that snow depths on canopy-free areas can be obtained accurately with the UAV photogrammetry.

Figure 9 Here

The mean snow density obtained from manual tube measurements is 0.355 g/cm^3 with a standard deviation of ±0.029 g/cm^3. The mean snow density estimated along transects is 0.364 g/cm^3 with standard deviation of ±0.069 g/cm^3. The average of the interpolated RSN is 0.365 g/cm^3 with standard deviation of ±0.074 g/cm^3. The results show that estimates of the average snow density from joint use of the GPR and UAV photogrammetry (0.364 g/cm^3) are in good agreement with those from manual tubes (0.355 g/cm^3) while the variation in the proposed model (±0.067 g/cm^3) is larger than of the snow tubes (± 0.029 g/cm^3). St. Clair and Holbrook (2017) achieved a similar accuracy (RMSE: ±0.050 g/cm^3) in their snow density observations with GPR system by observing hyperbolic diffractions in the radiograms for velocity estimations.

The mean snow water equivalent (SWE) obtained from manual tube is 366 mm, whereas the mean SWEs of transect and raster models are 384 mm and 391 mm, respectively. The results show that estimates of the average SWE from joint use of the GPR and UAV photogrammetry are in good agreement with those from manual tubes where the measurements are assumed as error-free. The RMSE of both transect and raster SWEs are ± 63 mm and ± 69 mm, respectively. The RMSE for the transect SWE and raster SWE relative to the mean SWE of the snow tube are 17% and 19%. St. Clair and Holbrook (2017) achieved a similar accuracy 12-21% in their SWE observations when they mounted the GPR on a ski mobile but their method is valid only if natural hyperbolic diffractions (likely a result of small boulders, small trees, bushes, or logs) are present, whereas in our approach this is not needed. The results show that estimating SWE from the UAV photogrammetry and GPR method combination gives spatially distributed SWE with an error of 17% and this is lower than the expected error of the proposed method, where the uncertainty in SD and uncertainty in TWT are independent to each other.

Table 3 Here

4 Discussions of the Results

Combining GPR and UAV photogrammetry based snow observation requires meticulous operational planning. Potential hazards of extreme winter conditions and related risks need to be assessed before performing snow surveys. If it is desired to have maximum snow thickness and water equivalent, it is necessary to take the snow observations for previous years into consideration. Attention should be paid to the presence of dry snow conditions to increase the accuracy of the radar measurements. GCPs should be preferred to establish the same locations for both summer and winter measurements. It would be much more useful to establish and mark stationary and pre-positioned GCPs to be routinely used in both winter and summer surveys for the same plot area. Such establishment would improve the uncertainty in georeferencing. To model the natural state of the snow cover, UAV measurements need to be made just before GPR measurements since the ski mobile may disturb the pristine snow. GPR acquisition rate and ski mobile speed may result in a range of very dense and very sparse sampling along the trajectory of the ski mobile so that the acquisition rate and travel speed need to be considered together in the survey plan. It is observed that the slope significantly decreases the spatial correlation of the snow density. Thus, GPR surveys need to be done, ideally, in parallel transects setting the appropriate spacing between the lines by considering the slope. The data acquisition rate for the ski mobile mounted GPR was 4 Hz while 1 Hz was used for the external GNSS. Hence, only a quarter of the GPR traces were matched up to the GNSS points. To avoid such inconsistency, GPR acquisition rate should be well synchronized to the external GNSS acquisition rate.

Slope effects were observed in places such as near road shoulders, where topography abruptly changes. Snow depths significantly increase at road margins. While average snow depth of the area was about 100 cm, road ditches have 142-160 cm snow depths showing that topographic fluctuations can significantly increase snow accumulations.

As the study area is composed of different land covers such as forests, individual trees, vegetation shrubs and bare ground in both sloping and flat areas, the study provides valuable insight into the value of UAV photogrammetry and GPR for snow characterization in diverse field conditions. Places where canopies were taller than snow depths appeared as individual trees or forests in both snow-free and snow-covered DSMs so that it was not possible to observe snow depths in such places. Snow depths and vegetation heights slightly decreased closer to trees. This is probably due to the effects of wind and interception from tree branches. In vegetation-covered areas, DSM differences (SDC) give only a part of the snow depth consisting of pure snow. The difference between snow-covered DSM and snow-free DTM (SDT) assesses the depths of the areas where vegetation is covered by snow. Snowflakes fills the gaps in the shrubs and plants as they fall. This situation leads to increments in snow depths. SDT estimates could be more meaningful and improve snow depth estimations if the formation of the snow-canopy mixture were properly modelled. However, there are some drawbacks from using a snow-free DTM instead of snow-free DSM. First, DTM pixel resolution is coarser than that of the DSM. Second, the DTM accuracy significantly decreases in large canopy-covered areas and in places having steep slopes. Third, the snow pack in the canopy-covered areas are mixed with canopies and snow.

In this study, manual snow measurements were assumed as true values although they inherently include some errors. Snow depths obtained from transect and raster surveys give excellent correlation with these manual measurements (Figure 9). However, poor correlation with density was obtained, despite good average estimates. Good correlation between estimated and measured SWE is apparent, although bias is evident (see Figure 9). We have assumed that the manual measurements are error free but, as discussed in the report of COST ES1404 action (HarmoSNOW, 2017), some variability in manual sampling is common. The Mountain Rose type tube, which was used to obtain snow measurements, may have bias in its balance, which would result in biased mass and density estimates

4. Conclusion

The main focus of this study was the investigation of a UAV photogrammetry-GPR integrated approach in obtaining spatially varied SWEs. Direct observations from snow tubes were chosen as a reference to assess the results. We have shown that the radar velocity in snowpack along transects can be calculated from GPR TWT and UAV snow depth measurements in the same study area. The use of spatially continuous snow depth data obtained from a UAV platform with spatially variable snow densities obtained from ski mobile GPR survey provides a map of SWEs. SWEs can be obtained reliably in less time with a UAV photogrammetry and GPR system than manual methods, although significant data processing is needed. It is known that the snow depth is typically more heterogeneous than the snow density, but as seen from the manual measurements reported here, snow density can also change significantly along a slope. Canopy cover affects the distribution of estimated snow depth and snowpack characteristics more compared to topography in the area studied here.

The study highlights the potential power of using a combined UAV photogrammetry and GPR method to study key snow properties. Because the spatial variability of SWE is driven more by variations in snow depth than in snow density, we suggest that SWEs derived from direct measurements of SD (from UAV photogrammetry) and interpolation of measured snow densities (from GPR survey) should be useful in validating/assimilating hydrological models. Although we have focused on a relatively small study area, the approach can be adopted at a larger area, thus offering immense value for basin-scale hydrology.

Data Availability

All data used during the study are available from the corresponding author by request.

References

Aki, K. and Richards, P.G., 1980. Quantitative seismology: Theory and methods, VII: W. H. Freeman Co.

Avanzi, F., Bianchi, A., Cina, A., Michele, C. De, Maschio, P., Pagliari, D.,Passoni, D., Pinto, L., Piras, M. & Rossi, L. (2018) Centimetric Accuracy in Snow Depth Using Unmanned Aerial System Photogrammetry and a MultiStation. Remote Sensing 10(5), 765. MDPI AG. https://doi:10.3390/rs10050765

Balanis, C. A., 1989, Advanced engineering electromagnetics: John Wiley & Sons, NY, 981p.

Beaumont, R.T. (1965). Mt. Hood Pressure Pillow Snow Gage. J. Appl. Meteor., 4, 626–631. https://doi.org/10.1175/1520-0450

Bentley, L.R. and Trenholm, N.M., 2002. The accuracy of water table elevation estimates determined from ground penetrating radar data: Journal of Environmental & Engineering Geophysics, 7, 37-53.

Bradford, J. H., Harper, J. T., & Brown, J. (2009). Complex dielectric permittivity measurements from ground-penetrating radar data to estimate snow liquid water content in the pendular regime: Water Resources Research. https://doi:10.1029/2008wr007341

Bradford, J. H., and Harper, J. T. (2005). Wave field migration as a tool for estimating spatially continuous radar velocity and water content in glaciers. Geophys. Res. Lett., 32, L08502, https://doi:10.1029/2004GL021770.

Bühler, Y., Adams, M. S., Bösch, R., and Stoffel, A. (2016). Mapping snow depth in alpine terrain with unmanned aerial systems (UASs): potential and limitations. The Cryosphere, 10(3), 1075-1088. https://doi.org/10.5194/tc-10-1075-2016

Capelli, A., Koch, F., Henkel, P., Lamm, M., Marty, C., & Schweizer, J., (2019). Snow water equivalent assessment with low-cost GNSS sensors along a steep elevation gradient. Geophysical Research, Vol. 21, EGU2019-15715, https://www.researchgate.net/publication/332934883

Church, J. (1933). Snow Surveying: Its Principles and Possibilities. Geographical Review, 23(4), 529-563. https://doi:10.2307/209242

Denoth, A., Foglar, A., Weiland, P., Mätzler, C., Aebischer, H., Tiuri, M., & Sihvola, A. (1984). A comparative study of instruments for measuring the liquid water content of snow: Journal of Applied Physics, 56, 2154–2160. https://doi:10.1063/1.334215

Dixon, D. & Boon, S. (2012). Comparison of the SnowHydro snow sampler with existing snow tube designs. Hydrol. Process., 26: 2555-2562. https://doi:10.1002/hyp.9317

Di Paolo, F., Cosciotti, B., Lauro, S.E., Mattei, E., Callegari, M., Carturan, L., Seppi, R., Zucca, F., & Pettinelli, E. (2015). Combined GPR and TDR measurements for snow thickness and density estimation, In Proceedings of the 8th International Workshop on Advanced Ground Penetrating Radar, Florence, Italy, 7-10 July 2015.

DJI Official. 2021a. Mavic Pro - Product Information - DJI. [online] Available at: <https://www.dji.com/mavic/info> [Accessed 30 March 2021].

DJI Official. 2021b. Phantom 4 - Product Information - DJI. [online] Available at: <https://www.dji.com/phantom-4/info> [Accessed 30 March 2021].

DJI, 2017a. Mavic Pro: User Manual V2, 2017-12. Retrieved from https://dl.djicdn.com/downloads/mavic/20171219/Mavic%20Pro%20User%20Manual%20V2.0.pdf

DJI, 2017b. Pahntom 4: User Manual V1, 2016-11. Retrieved from https://dl.djicdn.com/downloads/phantom_4/en/Phantom_4_User_Manual_en_v1.0.pdf

Dunse, T., Eisen, O., Helm, V., Rack, W., Steinhage, D. & Parry, V. (2008). Characteristics and small-scale variability of GPR signals and their relation to snow accumulation in Greenland's percolation zone, Journal of Glaciology, 54 (185), 333-342.

Eisen, O., Nixdorf, U., Keck, L., & Wagenback, D., (2003). Alpine ice cores and ground penetrating radar: combined investigations for glaciological and climatic interpretations of a cold Alpine ice body, Tellus B, 55(5), 1007-1017. https://doi:10.1034/j.1600-0889

Elder, K., Rosenthal, W., & Davis, R.E. (1998). Estimating the spatial distribution of snow water equivalence in a montane watershed: Hydrological Processes, 12, 1793–1808.

Feistl, T., Bebi, P., Dreier, L., Hanewinkel, M., & Bartelt, P. (2014). Quantification of basal friction for technical and silvicultural glide-snow avalanche mitigation measures, Nat. Hazards Earth Syst. Sci., 14, 2921–2931. https://doi:10.5194/nhess-14-2921-2014

Fomel, S., Landa, E., & Taner, M. T., (2007), Post-stack velocity analysis by separation and imaging of seismic diffractions: Geophysics, 72, no. 6, U89–U94. https://doi:10.1190/1.2781533

Forte, E., Dossi, M., Pipan, M. & Colucci, R.R. (2014). Velocity analysis from common offset GPR data inversion: Theory and application to synthetic and real data. Geophysical Journal International. 197. 1471-1483. 10.1093/gji/ggu103.

Gacitua, G., Bay, C., Pedersen, M.R., & Tamstorf, M.P. (2013). Quantifying snow and vegetation interactions in the high arctic based on ground penetrating radar (GPR): Arctic Antarctic and Alpine Research, 45, 201–210. https://doi:10.1657/1938-4246-45.2.201

Gray, D., Norum, D., & Dyck, G., (1970). Snow measurement in the prairie environment, *Canadian Agricultural Engineering*, vol. **12,** no. 1, 38– 41.

Godio, A. (2009). Georadar measurements for snow cover density, Am. J. Appl. Sci., 6, 414-423. https://doi:10.3844/ajas.2009.414.423

Goodison B, Glynn, JE., Harvey, K.D., & Slater, J.E. (1987). Snow surveying in Canada: A perspective. Canadian Water Resources Journal 12: 27−42.

Goodison B. (1978). Accuracy of snow samplers for measuring shallow snowpacks: an update. In Proceedings of the 35th Annual Meeting of the Eastern Snow Conference, Hanover New Hampshire, 36−49.

Gustafsson, D., Sundstrom, N., & Lundberg, A. (2012). Estimation of Snow Water Equivalent of Dry Snowpacks Using a Multi-Offset Ground Penetrating Radar System, 69th Eastern Snow Conference, Frost Valley YMCA, Claryville, New York, USA, 5-7 June 2012, 197-206, 2012.

Harder, P., Schirmer, M., Pomeroy, J., & Helgason, W. (2016). Accuracy of snow depth estimation in mountain and prairie environments by an unmanned aerial vehicle. The Cryosphere, 10, 2559–2571. https://doi.org/10.5194/tc-10-2559-2016

HarmoSnow, 2017. A European network for a harmonized monitoring of snow for the benefit of climate change scenarios, hydrology and numerical weather prediction. [online] https://harmosnow.eu/dissemination/reports/COST_2nd_field_campaign_report.pdf [Accessed 30 March 2021].

Harper, J. T., & Bradford, J. H. (2003). Snow stratigraphy over a uniform depositional surface: spatial variability and measurement tools, Cold Reg. Sci. Technol., 37(3), 289-298. https://doi:10.1016/S0165-232X(03)00071-5

Heilig, A., Eisen, O., & Schneebeli, M. (2010). Temporal observations of a seasonal snowpack using upward-looking GPR, Hydrol. Processes, 24, 3133–3145.

Holbrook, W.S., Miller, S. N., & Provart, M. A. (2016). Estimating snow water equivalent over long mountain transects using snowmobile-mounted ground-penetrating radar, Geophysics, 81(1), WA183-WA193, doi:10.1190/geo2015-0121.1.

Jenssen, R. O., Eckerstorfer, M., Jacobsen, S., and Storvold, R. (2019). Drone-Mounted Ultrawideband Radar for Retrieval of Snowpack Properties, in *IEEE Transactions on Instrumentation and Measurement*, vol. 69, no. 1, pp. 221-230, Jan. 2020. https://doi:10.1109/TIM.2019.2893043

Johnson, J.B., & Schaefer, G.L., (2002). The influence of thermal, hydrologic, and snow deformation mechanisms on snow water equivalent pressure sensor accuracy. Hydrol. Process., 16: 3529-3542. https://doi:10.1002/hyp.1236

Mitterer, C., A. Heilig, J. Schweizer, & O. Eisen. (2011). Upward-looking ground-penetrating radar for measuring wet-snow properties, Cold Regions Science and Technology, 69(2-3), 129-138. https://doi:10.1016/j.coldregions.2011.06.003

Moore, J., Pälli, A., Ludwig, F., Blatter, H., Jania, J., Gadek, B., Glowacki, P., Mochnacki, D., & Isaksson, E. (1999). High-resolution hydrothermal structure of Hansbreen, Spitsbergen, mapped by ground-penetrating radar. Journal of Glaciology, 45(151), 524-532. https://doi:10.3189/S0022143000001386

Marshall, H. P., Hoh, G., & Forster, R.R. (2005). Estimating alpine snowpack properties using FMCW radar, Ann. Glaciol., 40(1), 157– 162.

Mätzler, C., 1996. Microwave permittivity of dry snow. IEEE Transactions on Geoscience and Remote Sensing, vol. 34, no. 2, pp. 573-581, doi: 10.1109/36.485133.

Osterhuber, R. J., Gehrke F., & Condreva K. (1998). Snowpack snow water equivalent measurement using the attenuation of cosmic gamma radiation. 66th Annual Western Snow Conference, April 1998, Snowbird, Utah.

Pomeroy, J., & Gray, D. (1995). Snow cover. Accumulation, Relocation and Management. NHRI Science Report 7; NHRI: University of Saskatchewan, Canada; 134 pp.

Previati, M., Godio, A., and Ferraris, S. (2011). Validation of spatial variability of snowpack thickness and density obtained with GPR and TDR methods, J. Appl. Geophys., 75(2), 284-293. https://doi:10.1016/j.jappgeo.2011.07.007

Sold, L., Huss, M., Hoelzle, M., Andereggen, H., Joerg, P.C., & Zemp, M. (2013). Methodological approaches to infer end-of-winter snow distribution on alpine glaciers: Journal of Glaciology, 59, 1047–1059. https://doi:10.3189/2013JoG13J015

St. Clair, J. & Holbrook, W. S. (2017). Measuring snow water equivalent from common-offset GPR records through migration velocity analysis, The Cryosphere, 11, 2997–3009. https://doi.org/10.5194/tc-11-2997-2017

Tiuri, M., Sihvola, A., Nyfors, E. & Hallikaiken, M. (1984). The complex dielectric constant of snow at microwave frequencies, in IEEE Journal of Oceanic Engineering, vol. 9, no. 5, pp. 377-382, December 1984. https://doi:10.1109/JOE.1984.1145645

Webb, R. W., Jennings, K. S., Fend, M., & Molotch, N. P. (2018). Combining ground-penetrating radar with terrestrial LiDAR scanning to estimate the spatial distribution of liquid water content in seasonal snowpacks. Water Resources Research, 54, 10,339–10,349. https://doi.org/10.1029/2018WR022680

Webb, R.W. (2017). Using ground penetrating radar to assess the variability of snow water equivalent and melt in a mixed canopy forest, Northern Colorado. Front. Earth Sci. 11, 482–495, https://doi.org/10.1007/s11707-017-0645-0

Whitehead, K., Hugenholtz, C.H., Myshak, S., Brown, O., LeClair, A., Tamminga, A., Barchyn, T.E., Moorman, B., & Eaton, B. (2014). Remote sensing of the environment with small unmanned aircraft systems (UASs), part 2: Scientific and commercial applications1. Journal of Unmanned Vehicle Systems 02 (03): 86–102. https://doi.org/10.1139/juvs-2014-0007

Tables:

Table 1. Details about the applied unmanned aerial vehicles (UAV), camera systems, and flight and data acquisition parameters (DJI, 2017a; DJI, 2017b).

	Snow-free Survey	**Snow Survey**
UAV Details		
UAV type	DJI Mavic Pro	DJI Phantom-4
Dimensions	335 mm (diagonal size)	350 mm (diagonal size)
Weights	734 g	1380 g
Number of rotors	4 rotors	4 rotors
Stabilization	3-axis (pitch, roll, yaw)	3-axis (pitch, roll, yaw)
Max Speed	20 m/s	18 m/s
Max range	13 km (no wind)	7 km
Max flight time	27 minutes per battery	28 minutes per battery
Navigation sensors	GPS/GLONASS	GPS/GLONASS
Wireless Communication	1.1 GHz	2.4 GHz
Battery	3830 mAh LiPo 3S	6000 mAh LiPo 2S
Max wind speed	10 m/s	10 m/s
Camera Details		
Camera type	DJI FC220	DJI FC330
Sensor	1/2.3” CMOS	1/2.3” CMOS
Sensor resolution	4000x3000 (12 MP)	4000x3000 (12MP)
Lens	FOV 78.8° 26 mm	FOV 94° 20 mm
Aperture scale	f/2.2	f/2.8
ISO range	100-1600	100-1600
Color Mode	RGBs	RGBs
Flight and data acquisition Parameters		
Date	7 September 2017	5 February 2019
Begin of flight	09:15	14:08
Flight Duration	6 minutes	9 minutes
Side overlap	%75	%60
Forward overlap	%75	%80
Desired resolution	2.5 cm/pixel	3.5 cm/pixel
Flight height from ground	80 meters	150 meters
Temperature	18 °C	-1 °C (Sensible -3 °C)
Wind speed	3 km/h	4 km/h
Flight speed	6 m/s	12 m/s
Number of GCPs	11	8
Number of images	118	120
Covered Area	6 ha	49 ha

Table 2. Summary of the generated digital surface model (DSM) errors compared to the Global Navigation Satellite System (GNSS) measurements at ground control points (GCPs).

Flight Campaign	Number of Images	DSM Resolution (cm/pixel)	DTM Resolution (cm/pixel)	Orthophoto Resolution (cm/pixel)	X (cm) RMS Error	Y (cm) RMS Error	Z (cm) RMS Error	GCPs Used
Snow-free	118	2.7 x 2.7	13.7	2.7 x 2.7	±7.9	±5.7	±5.1	9
`Snow	120	5.8 x 5.8	29.5	5.8 x 5.8	±10.7	±12.5	±4.3	8

Table 3. Snow water equivalent (SWE) accuracies were evaluated based on manual snow measurements.

	Manual Survey	Transect Survey	Raster Survey
	Mean	Mean RMSE	Mean RMSE
Snow Depth (cm)	104	106 ±6	108 ±9
Snow Density (g/cm3)	0.355	0.364 ±0.069	0.365 ±0.074
Snow Water Equivalent (mm)	366	384 ±63	391 ±69

Figures

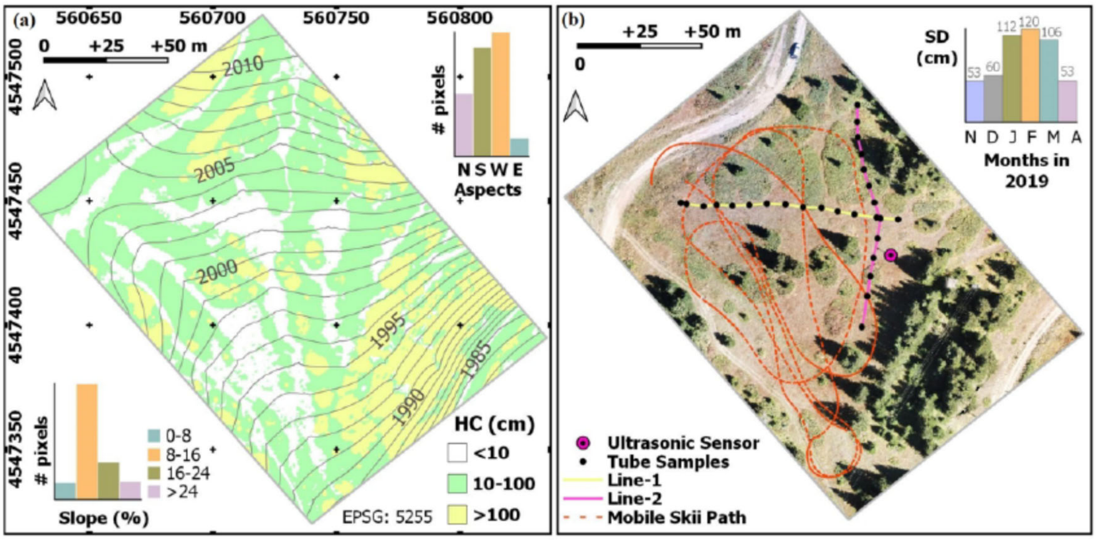

Figure 1. Map (a) shows 5 m contour lines and canopy heights (HC) along with slope and aspects histograms that were derived from UAV photogrammetry data. The map extents are limited to GPR survey extent though the UAV survey extents are larger. (b) shows outline of areas of interest for GPR data acquisition, as well as points where ultrasonic depth sensor and snow core (snow tube) measurements were performed. Line-1 (having %5 slope along WE direction) and Line-2 (having %12 slope along NS direction) are the transacts were GPR survey were pulled by operator. Mobile ski path shows the positions of the ski mobile mounted GPR survey. The base map is the orthophoto of the plot area derived from UAV photogrammetry survey.

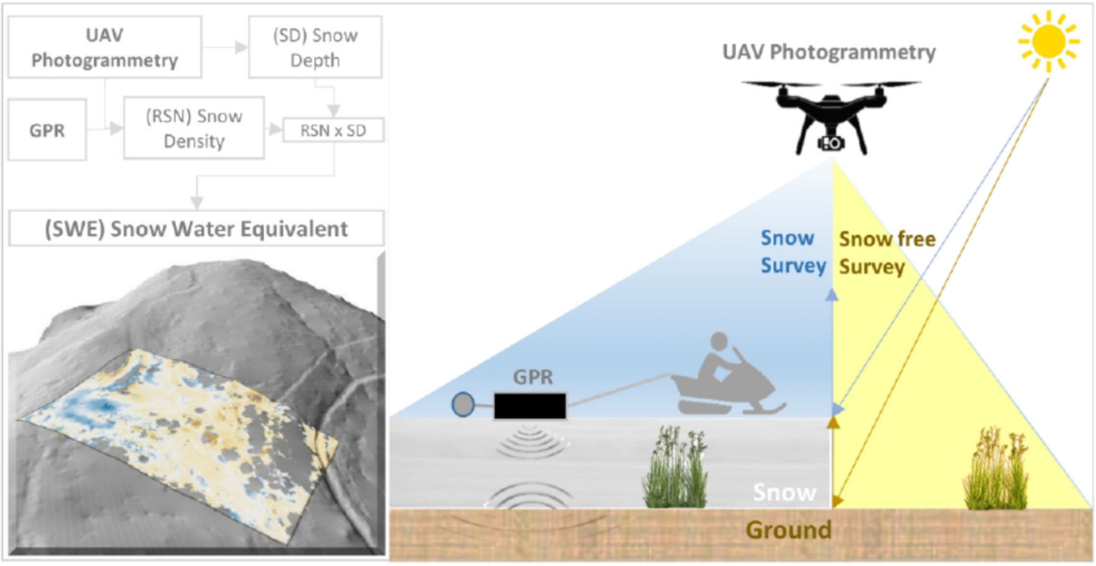

Figure 2. A basic graphical representation of the proposed model. Spatially continues snow depths (SD) were obtained from two successive UAV based photogrammetric surveys (in snow-free and snow-covered conditions respectively). Then, GPR two-way travel times of the snow ground/interface and obtained snow depths were used to calculate spatially continues snow densities (RSN) along GPR transects. Finally, spatially continues snow water equivalents (SWE) of the plot area were obtained from multiplication of the SD and spatially interpolated RSN values. 3-D view of the SWE draped over the hillshade of the snow-free digital terrain model (left bottom panel).

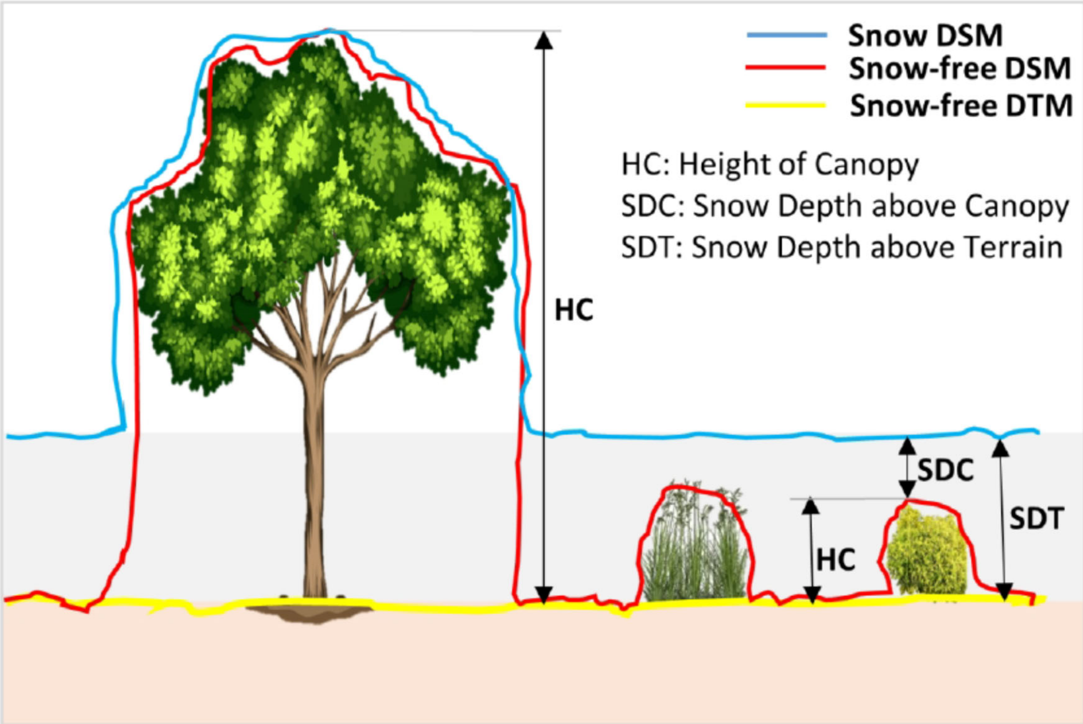

Figure 3. Illustration of the height of the canopy (HC), snow depth above canopy (SDC) and snow depth above terrain (SDT) obtained from photogrammetric surface models (DSMs and DTM).

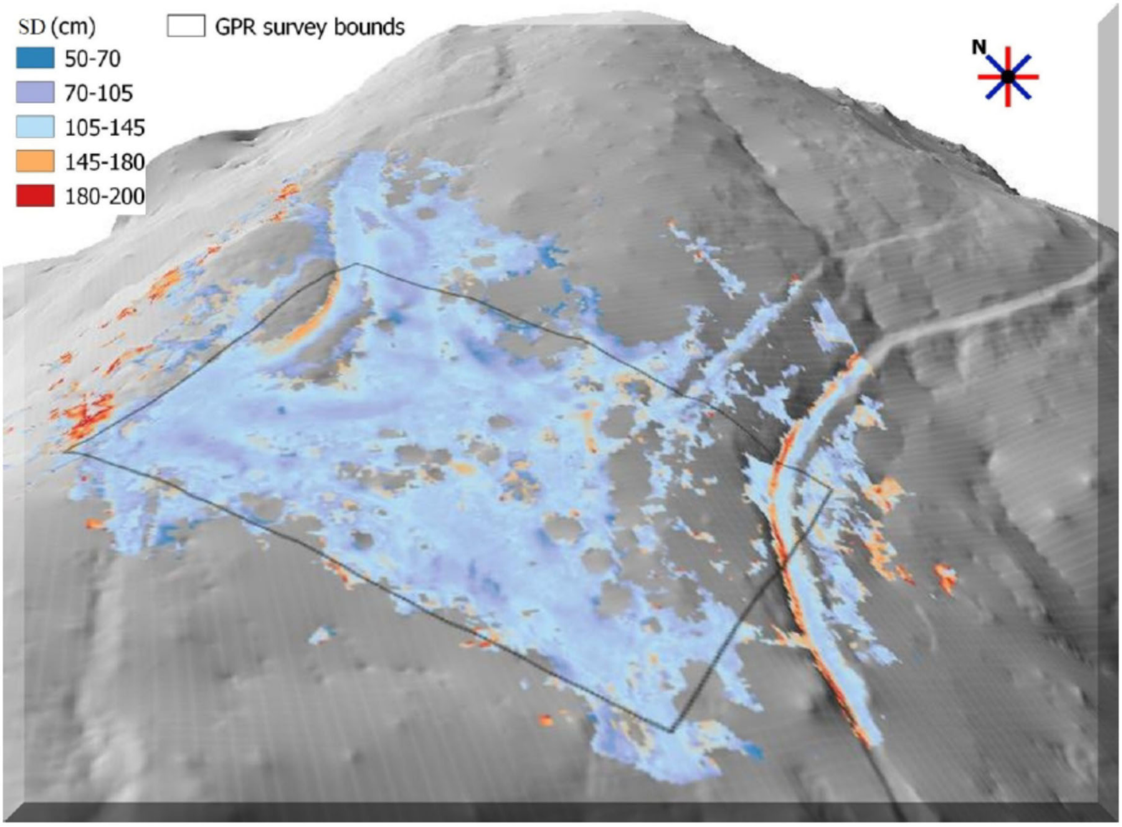

Figure 4. 3-D view of the snow depths (SD) draped over the hillside of the snow-covered DSM facing from northeast to southwest.

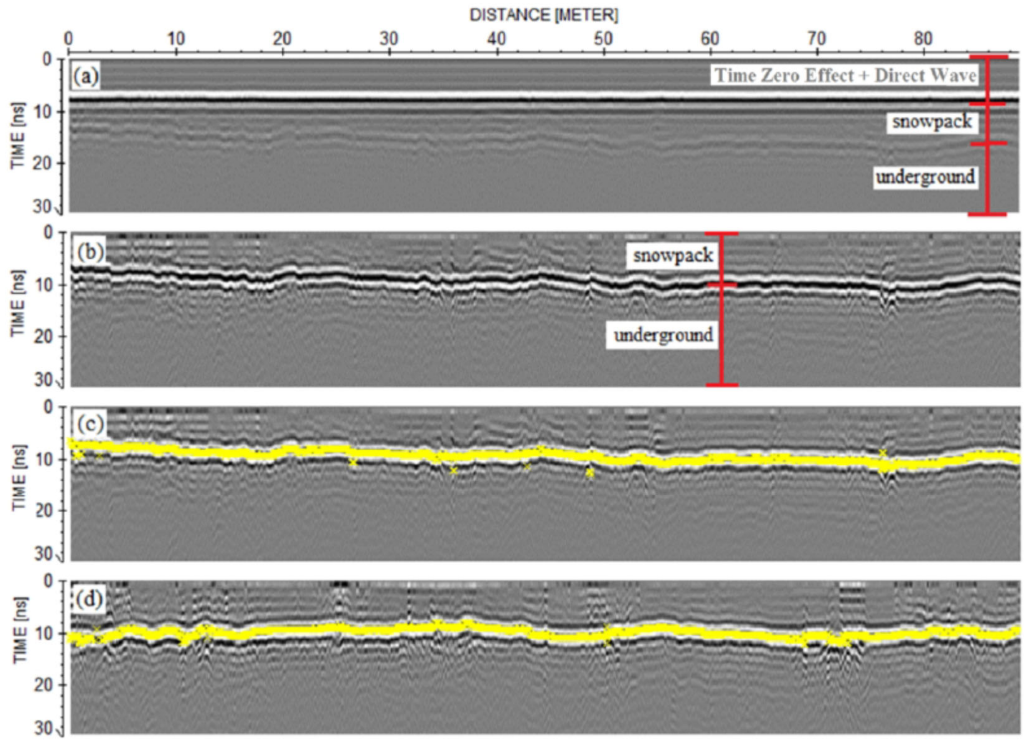

Figure 5. Panel (a) is the raw GPR data collected along Line-1 having three observable layers (direct wave and time zero effect, snow, and underground). The upper air layer and time zero effect was removed, the snow and ground layers were highlighted by applying suitable processing techniques. The final processed profiles exhibit very clear snow-ground reflections as shown on the panel (b) for Line-1. TWTs of the snow layers were picked based on snow-ground reflections (yellow lines). Panel (c) and panel (d) show the picked reflections along Line-1 and Line-2, respectively.

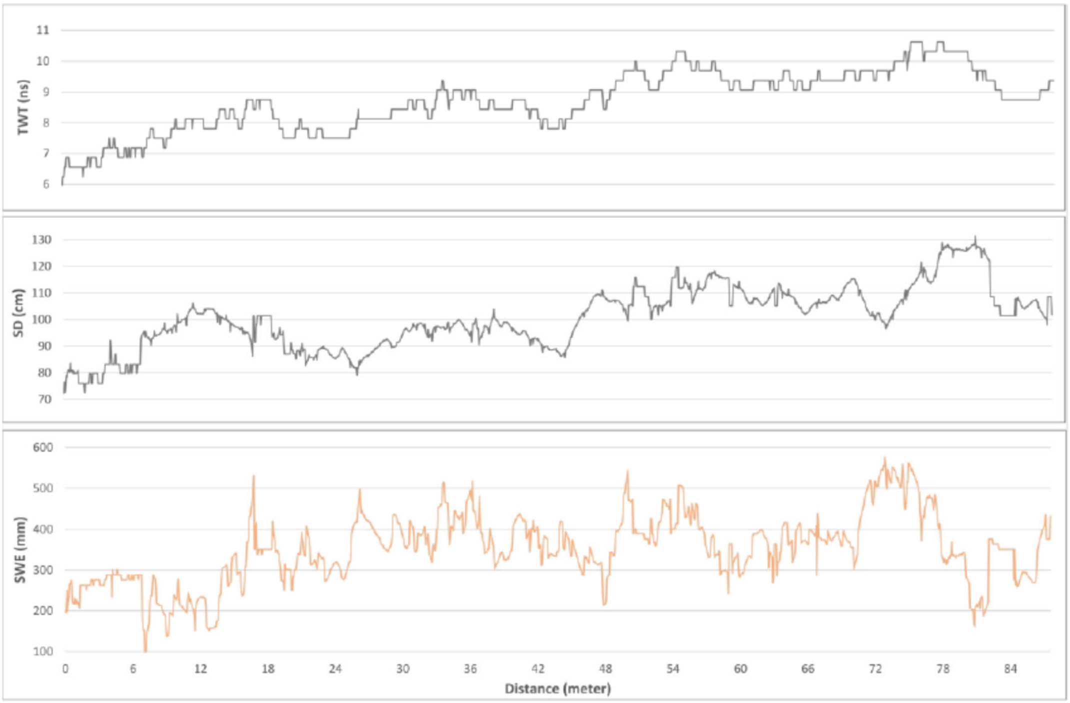

Figure 6. GPR two-way travel times (TWT) were measured by GPR systems along Line-1. Snow depths (SD) along Line-1 were obtained from UAV photogrammetry. TWT and SD were then used to calculate snow water equivalents (SWEs). The graphs show that the spatial variability of SWEs are higher than that of its components (TWT and SD).

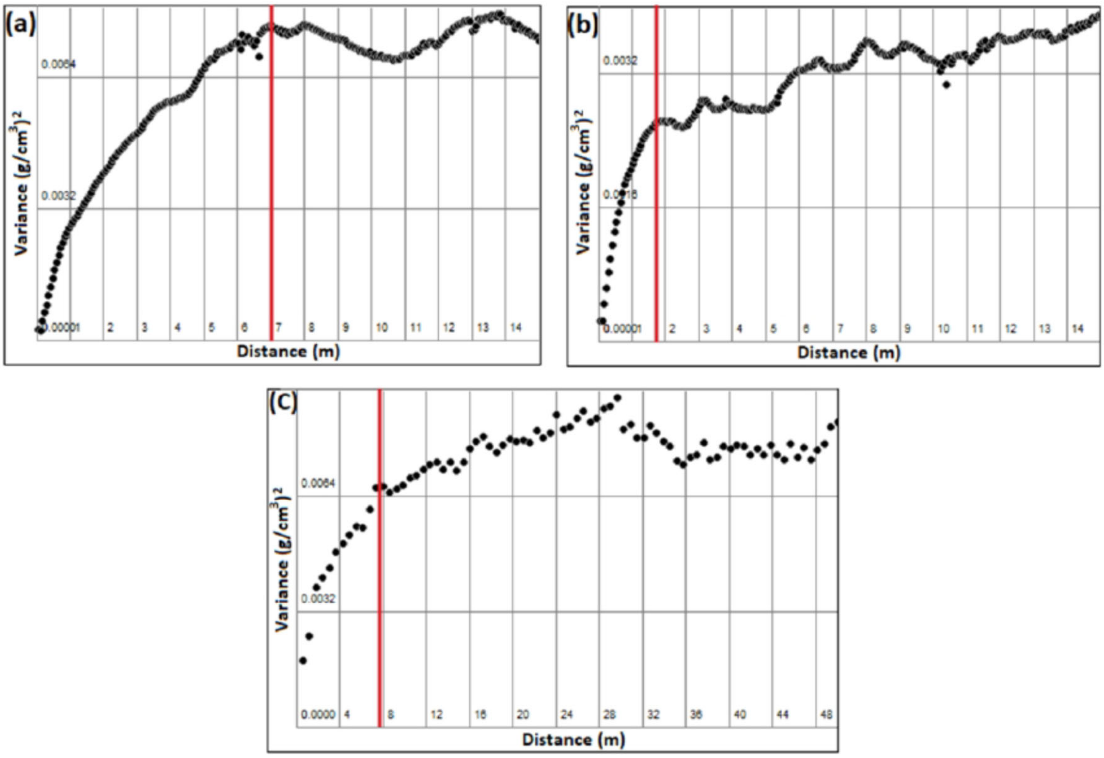

Figure 7. Variograms of the snow densities obtained from joint use of GPR and UAV photogrammetry along Line-1 (a), Line-2 (b) and Ski Mobile Path (c). The range distances show that snow densities are geospatially correlated within 7 meters for Line-1, 1.8 meters for Line-2 and 7.8 m for Ski Mobile Path.

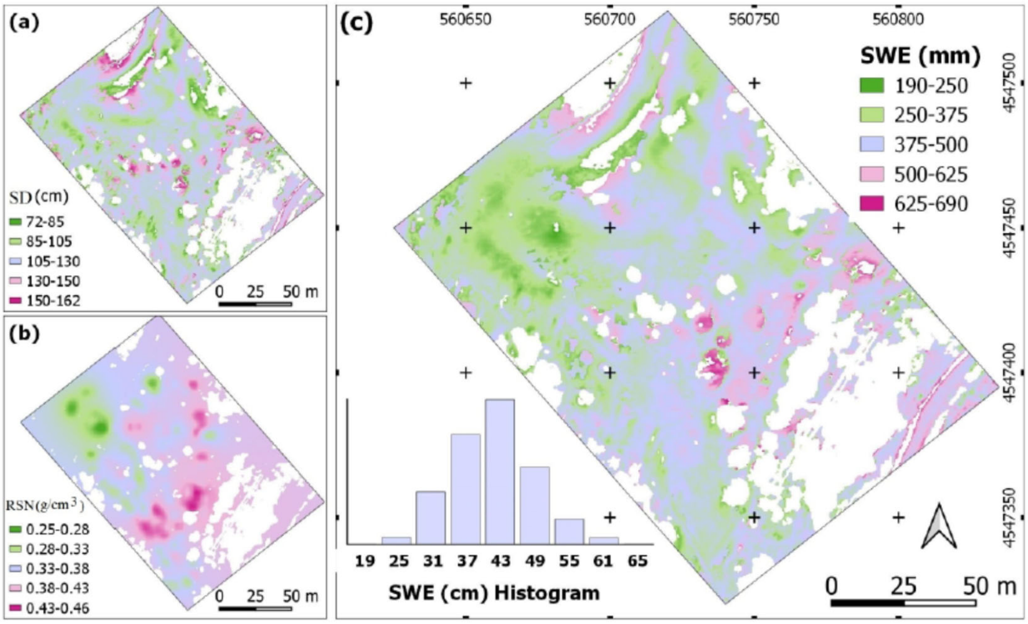

Figure 8. SD map of the plot area were created as shown on the panel (a). Transects snow densities were mapped to the plot area using inverse distance interpolation (IDW) algorithm as shown on the panel (b). Raster snow water equivalents (SWE) were calculated from SD and RSN, panel (c). The SWE values are in range of 19 mm and 690 mm showing high spatial variability. The histogram of the SWE map is also shown the panel (c).

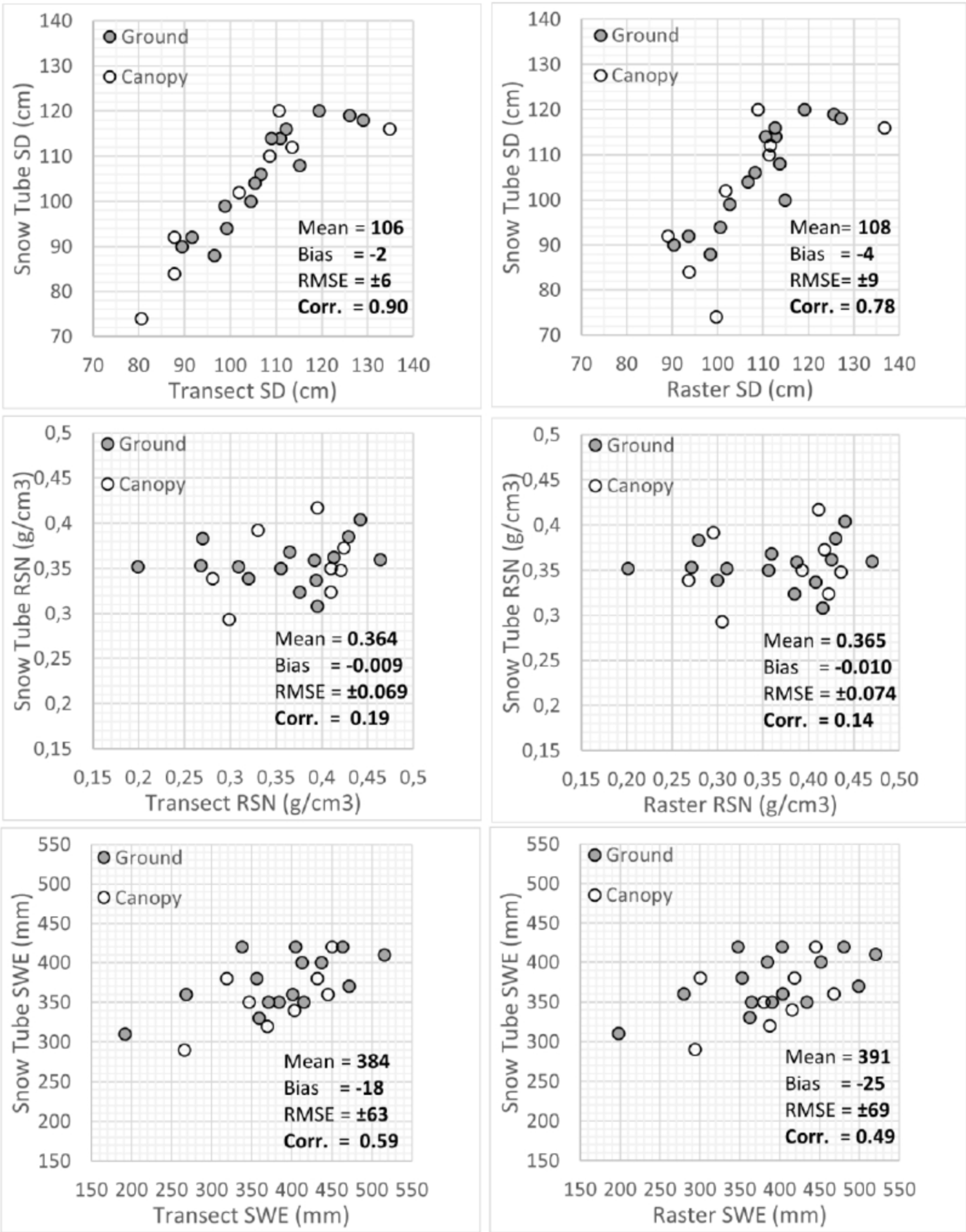

Figure 9. Snow depths (SD), snow density (RSN) and snow water equivalent (SWE) measurements both along transects and throughout the survey area (raster) were compared with manual snow tube (snow core) measurements for 23 different points. The points were also colored whether they are located on canopies or not.